Journal of *Marine Science and Engineering*

MDPI

Article

The Asynchronous Installation Effect on the Embedment Performance and Dynamic Response of a Novel Group-Drag-Anchor System in a Soft Clay Seabed

Yancheng Yang [1,2,*], Yifeng Lin [1] and Dezhi Ning [2]

[1] Shanghai Investigation, Design & Research Institute Co., Ltd., Shanghai 200335, China
[2] State Key Laboratory of Coastal and Offshore Engineering, Dalian University of Technology, Dalian 116024, China
* Correspondence: yych110a@163.com

Abstract

A novel group-drag-anchor system (GDAS), comprising a Delta anchor and a four-tooth anchor, was developed to enhance mooring capacity for floating offshore wind turbines in soft clay seabeds. This study focuses on the influence of the installation method on the embedment performance and dynamic response of the GDAS. Large-deformation finite element analyses were conducted using the coupled Eulerian–Lagrangian (CEL) technique to simulate the installation process under different configurations. A dedicated subroutine was implemented to monitor the evolution of excess pore pressure around the GDAS during the subsequent dynamic loading. Results show that asynchronous installation yields significantly deeper embedment than synchronous installation, especially in seabeds with steep strength gradients. The dynamic response of the GDAS under wave-only, combined wave–current, and mooring-line-failure loading scenarios was further investigated. The asynchronously installed GDAS exhibits considerably more stable long-term performance and lower risk of progressive failure under extreme environmental conditions. This superiority is most evident in clays with a relatively steep strength gradient. These findings provide valuable guidance for the optimal design and installation sequencing of GDASs in engineering practice.

Keywords: group-drag-anchor system; large deformation analyses; soft clay; ultimate embedment depth; dynamic response; installation trajectory

Check for updates

Academic Editor: Spyros A. Mavrakos

Received: 28 January 2026
Revised: 19 February 2026
Accepted: 25 February 2026
Published: 27 February 2026

Copyright: © 2026 by the authors. Licensee MDPI, Basel, Switzerland. This article is an open access article distributed under the terms and conditions of the Creative Commons Attribution (CC BY) license.

1. Introduction

Drag anchors are efficient mooring solutions for floating offshore wind turbines (FOWTs) due to their high horizontal bearing capacity. However, as turbine size and capacity rapidly increase, single anchors often lack sufficient holding capacity, particularly in soft seabeds [1,2]. While drag-anchor designs have evolved substantially over recent decades, further structural refinements are yielding diminishing returns [3–5]. Compared to conventional plate anchors, group-drag-anchor systems (GDASs) offer distinct advantages in terms of bearing performance, application scope, and cost-effectiveness. Experimental studies show that well-designed GDASs can achieve more than twice the bearing capacity of individual anchors, as the back anchor attains significantly deeper embedment [2,6–12]. Despite this potential, research on them remains limited, particularly for configurations using non-identical components. To address this, a novel GDAS concept was proposed to optimize anchor selection, connection methods, and sizing for enhanced system efficiency [13].

The superior bearing efficiency of drag anchors arises primarily from their ability to achieve deep embedment depths, making ultimate embedment a key performance indicator in engineering practice. Numerous experimental and numerical studies have been conducted to understand embedment behavior [14–26]. Complementing these efforts, theoretical and semi-analytical predictive models have been progressively refined over several decades [6,27–31]. These studies have provided robust tools for analyzing the installation trajectories and capacity of conventional single drag anchors. Despite such progress, significant knowledge gaps remain regarding the installation mechanics and ultimate embedment of GDASs, particularly those incorporating diverse anchor components. Although an innovative GDAS configuration was recently proposed and demonstrated its superior diving performance under selected seabed conditions through systematic numerical studies [13], the influences of varying installation techniques and soil profiles on its long-term behavior remain unexplored.

The long-term dynamic response of anchors has also garnered substantial attention [32,33]. Investigations emphasize the pivotal role of soil–anchor interactions under cyclic and impact loading, particularly in saturated soils, where pore water pressure accumulation intensifies alongside large-scale deformation. A more thorough understanding of the flow-around mechanism under these conditions is essential for reliable prediction of residual bearing capacity. Partially installed drag anchors were assumed to embed deeper when subjected to extreme overloads [34], thereby recovering or even enhancing their ultimate capacity. As a result, a tool for tracking the development of the displacement and the capacity of the anchor for a given loading history is required. A fully coupled numerical model for floating offshore wind turbines (FOWTs) was developed, demonstrating that the equivalent damping arising from anchor–chain–soil interactions varies with excitation amplitude and period [35]. Traditional models, which impose fixed boundaries at mooring line embedment points, overestimate the mooring system's restoring stiffness, thereby underestimating FOWT surge and sway responses by approximately 30%. However, the dynamic response of GDASs under environmental loads, such as waves and currents, remains a sparsely examined frontier, marked by a dearth of empirical and analytical studies.

This paper systematically investigates the influence of asynchronous installation on the performance of the novel GDAS comprising a four-tooth anchor and a Delta anchor in a soft seabed. Using a validated coupled Eulerian–Lagrangian (CEL) approach, both the installation process and the subsequent dynamic response of the system are simulated. Four asynchronous installation levels are investigated to explore the effect on the embedment depth of the GDAS. The ultimate embedment depths under varying asynchronous conditions are compared. The underlying mechanisms are analyzed. Additionally, the dynamic responses of the GDASs installed by diverse asynchronous installation conditions under wave-only, combined wave–current and line-failure loading conditions are investigated by introducing a subroutine code that can monitor the real-time evolution of excess pore pressure around the system. The potential failure mechanisms under extreme environmental loads are identified and analyzed in depth. The findings offer valuable insights for optimizing GDAS installation strategies in offshore engineering applications.

2. Numerical Model

This section outlines the numerical framework employed to investigate the asynchronous installation and dynamic response of the GDAS (Figure 1). Large-deformation analyses were performed using the CEL technique implemented in Abaqus 2018/Explicit.

A comprehensive convergence study was first conducted to determine the optimal model domain and mesh resolution to achieve a balance between computational efficiency and solution accuracy. The soil was modeled with an advanced constitutive formulation

incorporating strain-softening and strain-rate effects, both of which are critical for accurately capturing the installation and cyclic responses of soft clays.



Figure 1. Novel group-drag-anchor system (a scaled model photographed by the authors).

Additionally, a hydro-mechanically coupled CEL method was developed using a thermal-poro-mechanical analogy in a VUMAT subroutine. This approach was validated against two free-fall piezocone penetration tests, demonstrating excellent agreement in both penetration depth and excess pore-pressure variation.

2.1. Constitutive Model Considering Soil Strain-Softening and Strain-Rate Effects

The soil is modeled using an extended Tresca constitutive framework that incorporates strain-softening and strain-rate effects, following the formulation in Reference [36]. The undrained shear strength at any material point evolves according to:

$$s_u = \beta_s \beta_r s_{ui} \tag{1}$$

where s_{ui} is the initial undrained shear strength of soil and β_s and β_r are the softening and strain-rate coefficients, respectively, defined as:

$$\beta_s = \delta_{rem} + (1 - \delta_{rem}) e^{-3\xi/\xi_{95}} \tag{2}$$

$$\beta_r = 1 + \mu_{10} \lg\left(\max(|\dot{\gamma}_{max}|, \dot{\gamma}_{ref})/\dot{\gamma}_{ref}\right) \tag{3}$$

where δ_{rem} denotes the inverse of the soil sensitivity S_t, ranging from 0.01 to 1.0; ξ_{95} is the cumulative plastic strain at which soil strength decreases by 95%; ξ represents the current cumulative plastic strain of soil; $\dot{\gamma}_{max}$ is the maximum shear strain rate at the current increment step; $\dot{\gamma}_{ref}$ is the reference shear strain rate; and μ_{10} represents the soil-strength growth rate per decade, typically ranging from 0.05 to 0.2 for lightly overconsolidated clays. These parameters are updated at each integration point through the VUMAT subroutine. To verify the implementation, a single soil element is subjected to strain-controlled two-way cyclic shearing for a period of 6 s, referencing the value for a typical storm load suggested in Reference [36]. The numerical predictions are compared with the corresponding analytical solutions, as shown in Figure 2, and show excellent agreement.

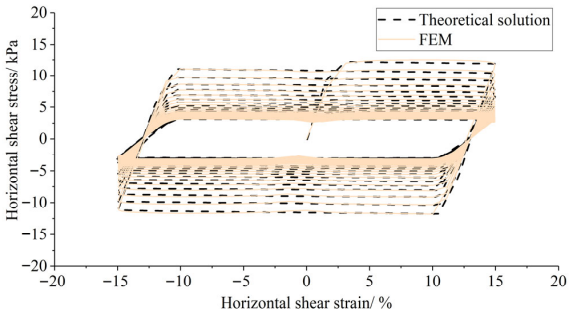


Figure 2. Tresca model considering strain-softening and strain-rate effects.

2.2. Numerical Model and Convergence Study

An explicit time integration scheme was adopted, with its stability guaranteed by a critical time step increment calculated as $\Delta t_c = \min(L_e/c_d)$, where L_e denotes the characteristic element dimension, while c_d represents the dilatational wave speed of the material. A void layer was positioned above the soil surface to facilitate the free flow of clay. The soil-strength profile follows $s_u = s_{u0} + 0.5z$ kPa, where z is the depth below the mudline, and s_{u0} is the undrained shear strength of soil at the mudline. The constitutive model detailed in Section 2.1 was employed for the analysis. The elastic properties of the soil were defined as Young's modulus $E = 500\ s_u$ and Poisson's ratio $\mu = 0.49$ for incompressible behavior [37]. The coefficient of earth pressure K_0 was assigned a value of 1.0 to simulate an isotropic initial stress state. Interaction between Eulerian and Lagrangian materials utilizes a "hard contact" model with a friction coefficient μ_0 of 0.2.

The mooring-line tension at the mudline is prescribed as a known time history, and the corresponding tension and inclination at the padeye of the GDAS are computed in real time using the analytical chain equation in Reference [38], as follows:

$$-[T_a/(1+\mu_l^2)][e^{\mu_l(\theta_{ah}-\theta)}(\cos\theta+\mu_l\sin\theta)_{\theta_e}^{\theta_{ah}}] = \int_{z_e}^{z_a} N_{cl}E_n d_l s_u dz \quad (4)$$

where θ_{ah} is the angle between the drag force at the padeye and the horizontal plane; θ_e is the loading angle of the cable at the mudline relative to the horizontal plane; θ is the angle formed by the cable relative to the horizontal plane; N_{cl} is the bearing capacity factor of the anchor chain or cable; E_n is the multiplier that depends on the anchor line property, with E_n = 2.5 for chains and E_n =1.0 for cables; d_l is the diameter of the anchor chain or cable; s_u is the undrained shear strength of the soil; T_a represents the drag force applied at the padeye; μ_l is the frictional coefficient between the soil and the anchor cable; and z_e denotes the initial embedment depth of the loading chain due to the self-weight of the chain, which can be expressed by $z_e = w/(kN_{cl}b) - s_{u0}/k$. Here, w is the submerged line weight per unit length. Within each analysis increment, the VUAMP user subroutine solves Equation (4) iteratively to update the magnitude of the drag force T_a and drag angle θ_{ah}. This dynamic updating ensures accurate representation of the evolving load and direction throughout the entire drag-embedment and subsequent dynamic-loading phases. Figure 3 illustrates the detailed numerical solution procedure. In this framework, the horizontal and vertical components of the mooring-line tension are computed within the VUAMP subroutine, while the padeye coordinates are updated directly in the main Abaqus code. In all numerical analyses, a target control velocity v_c is prescribed. Rather than applying a constant force, the drag force is dynamically modulated using a servo control algorithm to maintain this constant velocity. The incremental adjustment to the drag force, ΔT, is proportional to the normalized velocity deviation and is given by $\Delta T = (v_c - \overline{v})/v_c$ kN, where $\overline{v}$ is the mean horizontal velocity. The control velocity was set at 0.1 L_f/s. An error tolerance of 1 e^{-5} was adopt for the iterative calculation of drag angle θ_{ah}. The value t_c is set at 0.001, as recommended in Reference [39].

Boundary effects and mesh convergence were investigated for the installation and cyclic-loading phases of the GDAS analyses.

For the installation process, Figure 4a depicts the model domain, where the width was systematically varied to minimize boundary effects. In the previous study, the associated convergence study indicated that results stabilize once the domain width reaches 10 L_f, with a mean deviation of only 1.71% relative to the 12 L_f case [13]. Accordingly, a domain width of 10 L_f was adopted for all subsequent installation analyses. To fully capture the anchor's trajectory, the domain length and depth were set to 55 L_f and 10 L_f, respectively. Mesh refinement studies indicated that further reduction in the minimum element size

below $L_f/10$ produced negligible improvement, with a mean deviation of just 2.89% relative to an $L_f/12$ refinement [13]. This resolution is also in line with recommendations from earlier CEL investigations of drag anchors [40]. Thus, a minimum mesh size of $L_f/10$ was employed for the subsequent installation analyses.

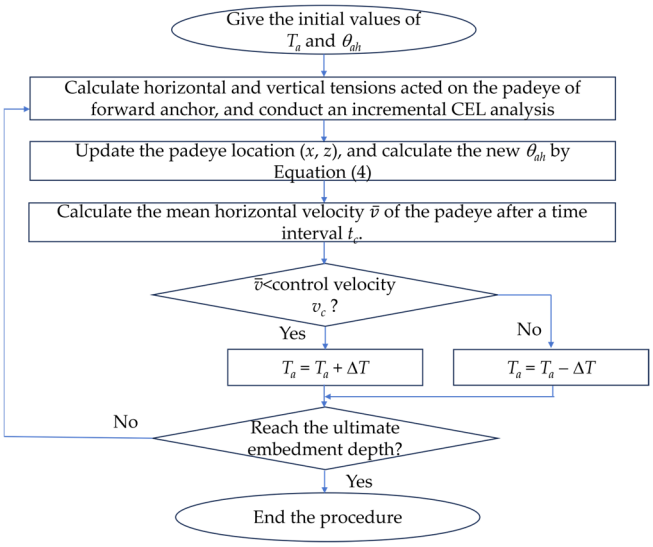


Figure 3. Procedure of the numerical solution.

During the cyclic load phase, a regular cyclic tension with a frequency of 0.05 Hz and a mean value of 9354.8 kN was applied at the mudline. This cyclic load is selected as a relatively high amplitude and frequency load to sufficiently eliminate the boundary effect of the model domain, whose determination process will be introduced in detail in the subsequent section (Section 3.2). Figure 4c,d compare the displacement results of the GDAS for domain widths of 8 L_f, 12.7 L_f and 17.5 L_f. Displacement response converges satisfactorily once the width exceeds 12.7 L_f. To ensure the calculation accuracy and eliminate residual boundary effects, the model domain with a width of 17.5 L_f was adopted for all subsequent cyclic analyses. The length of the domain L_s is 40 L_f to eliminate the boundary effect. As shown in Figure 4e,f, mesh-refinement studies confirmed that reducing the minimum element size below L_f /13 yields negligible improvements. Therefore, a minimum element size of L_f /13 was employed for all cyclic-loading simulations.

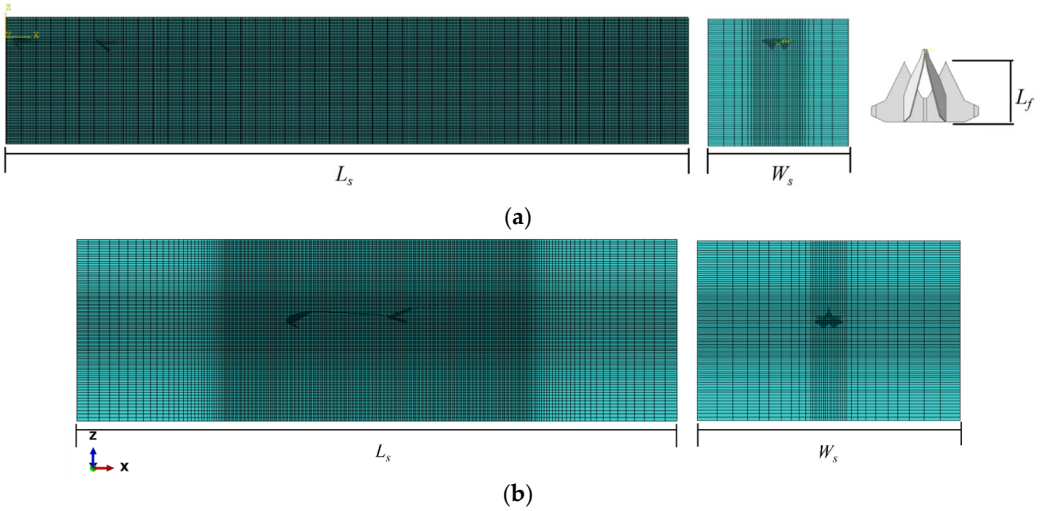


Figure 4. *Cont.*

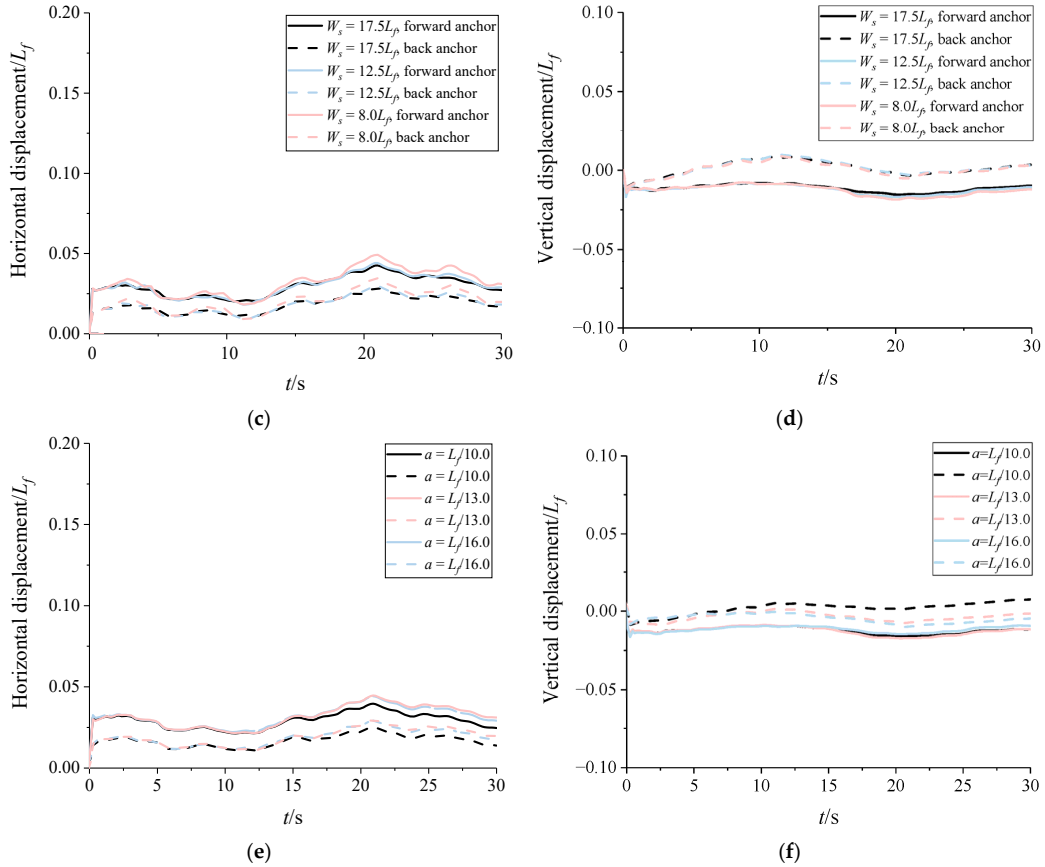


Figure 4. Domain and convergence of domain width of the CEL model: (**a**) model domain and meshes (installation process); (**b**) model domain and meshes (operational state); (**c**) convergence of GDAS's horizontal displacement on domain width; (**d**) convergence of GDAS's vertical displacement on domain width; (**e**) convergence of GDAS's horizontal displacement on mesh size; and (**f**) convergence of GDAS's vertical displacement on mesh size.

2.3. The Hydro-Mechanically Coupled CEL Method

The hydro-mechanically coupled CEL method is realized by the VUMAT subroutine, where the balance equations for the hydro-mechanically coupled problem are introduced. A hydro-mechanically coupled CEL method suitable for simulations involving slow processes without high accelerations on the Abaqus platform was first developed in Reference [41], where the thermal–mechanical analysis is applied to eliminate the need for dedicated pore-pressure elements in the numerical modeling framework. After that, this method was extended to arbitrary problems, involving high acceleration problems [42]. For the hydro-mechanically coupled problems, the u-p formulation proposed in Reference [43] is applied. The mass balance of the pore fluid is expressed by

$$\varphi^f \frac{1}{\overline{K}^f} \dot{p}^f + \varphi^f \mathrm{div}(\dot{u}^f) + (1 - \varphi^f)\mathrm{div}(\dot{u}^s) = 0 \tag{5}$$

where $\dot{u}^s$ and $\dot{u}^f$ denote the velocities of the solid and pore fluid, respectively; $\overline{K}^f$ represents the bulk modulus of the fluid; φ^f denotes the volume fraction of the pore fluid; and $\dot{p}^f$ is the increasing rate of pore fluid pressure. Here, the pore fluid velocity $\dot{u}^f$ is unknown. The Darcy velocity of the pore fluid w^f has the following relationship with $\dot{u}^s$ and $\dot{u}^f$,

$$w^f = \varphi^f(\dot{u}^f - \dot{u}^s) \tag{6}$$

The permeability follows the isotropic and constant assumptions. In the u-p formulation framework, the balance of the linear momentum of the pore fluid can be expressed by,

$$w^f = \frac{K^{\mathrm{Perm}}}{\eta^f}[-\mathrm{grad}(p^f) + \overline{\rho}^f(g - \ddot{u}^s)] \tag{7}$$

where $\overline{\rho}^f$ denotes the intrinsic density of the fluid; $\ddot{u}^s$ is the acceleration of the solid; K^{Perm} is the permeability of the solid; η^f represents the dynamic viscosity of the fluid; g is the gravity; and p^f is the pore fluid pressure. In Equation (7), the assumption is that the accelerations of the solid $\ddot{u}^s$ and pore fluid $\ddot{u}^f$ are identical. The validity of the assumption to the problems involving the high wave frequencies and high hydraulic conductivity of soil is questioned. The influence of the relative acceleration was studied and it was found that when the hydraulic conductivity was lower than 10^{-3} m/s and the frequency was lower than 55 Hz, the influence could be negligible [42]. Their findings indicate that the influence of the relative acceleration is negligible for most offshore geotechnical applications and the u-p formulation is valid.

Equation (7) is substituted into Equation (5) resulting in,

$$\varphi^f \frac{1}{\overline{K}^f}\dot{p}^f + \mathrm{div}\left\{\frac{K^{\mathrm{Perm}}}{\eta^f}[-\mathrm{grad}(p^f) + \overline{\rho}^f(g - \ddot{u}^s)]\right\} + \mathrm{div}(\dot{u}^s) = 0 \tag{8}$$

The similarity between the energy balance for thermal process simulation and Equation (8) is used to incorporate the hydro-mechanically coupled method in Abaqus. The energy balance satisfies the following equation,

$$\rho c\dot{\theta} + \lambda \mathrm{div}[-\mathrm{grad}(\theta_T)] = -\dot{m}_T \tag{9}$$

where c is the specific heat; θ_T is the temperature; λ represents the thermal conductivity; ρ is the total density; and $\dot{m}_T$ is the production of internal heat. Equation (8) can be further rewritten as follows, with the relationship of $\overline{\rho}^f g - \mathrm{grad}\left(\rho^f\right) = -\mathrm{grad}(\Delta\rho^f)$,

$$\varphi^f \frac{\Delta\dot{p}^f}{\overline{K}^f} + \frac{K^{\mathrm{Perm}}}{\eta^f}\mathrm{div}[-\mathrm{grad}(\Delta p^f)] - \frac{K^{\mathrm{Perm}}}{\eta^f}\mathrm{div}(\ddot{u}^s) + \mathrm{div}(\dot{u}^s) = 0 \tag{10}$$

By interpreting the temperature as the excess pore fluid pressure, according to the similarity between the energy balance for thermal and hydro-mechanically, three matching items can be identified as follows,

$$\rho c\dot{\theta}_T = \frac{\varphi^f}{\overline{K}^f}\Delta\dot{p}^f \tag{11}$$

$$\lambda \mathrm{div}[-\mathrm{grad}(\theta_T)] = \frac{K^{\mathrm{Perm}}}{\eta^f}\mathrm{div}[-\mathrm{grad}(\Delta p^f)] \tag{12}$$

$$\dot{m}_T = -\frac{K^{\mathrm{Perm}}}{\eta^f}\mathrm{div}(\ddot{u}^s) + \mathrm{div}(\dot{u}^s) \tag{13}$$

where the specific heat c and the thermal conductivity λ are set as constants in the thermal-displacement analysis in Abaqus. Their values are set to,

$$c = \frac{\varphi^f}{\rho\overline{K}^f} \tag{14}$$

$$\lambda = \frac{K^{\mathrm{Perm}}}{\eta^f} \tag{15}$$

The heat production $\dot{m}_T$ is defined in the VUMAT subroutine code, as expressed in Equation (13).

This approach is suitable for saturated soil, and assessment is required for unsaturated conditions.

2.4. Linking Chain Configuration of GDAS

Asynchronous installation is a novel concept designed to leverage the "asynchronous effect" to enhance GDAS performance. This can be realized by the strategic configuration of initial spacing, triggering force or activation time. In this study, the initial spacing is adopted to regulate the asynchronous degree, as it represents the most straightforward method. In practical offshore operations, the initial spacing of the GADS can be managed using an offshore construction lifting vessel and an underwater robot, as shown in Figure 5. The initial anchor spacing is shorter than the chain length, leaving the chain slack until dragging extends the spacing to match the chain length. For the force-controlled approach, a connector between anchor components can be engineered with a predefined breaking strength to control the asynchronous installation triggering condition, so the GDAS can be separated. Additionally, a time-controlled approach is implemented by modulating the drag velocity of the anchor handling vessel (AHV). By adjusting the vessel's speed prior to the tensioning of the connecting chain, the timing of the GDAS's deployment can be staggered as required.

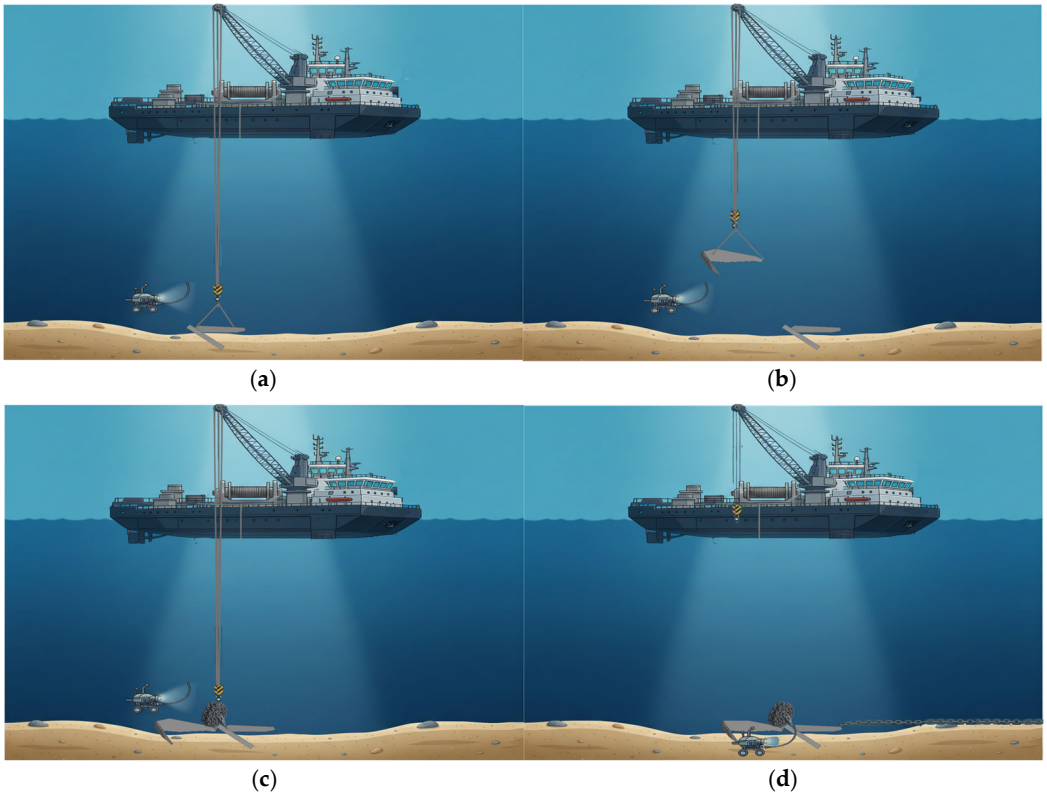


Figure 5. Deployment of GDAS for asynchronous installation: (**a**) deployment of forward anchor; (**b**) deployment of back anchor; (**c**) deployment of linking chain; and (**d**) connecting linking chain by underwater robot.

To achieve synchronous or asynchronous installation, the linking chain layout is varied, as shown in Figure 6a. Synchronous installation requires the initial anchor spacing

to match the chain length, ensuring immediate tensioning. This ensures the chain tightens immediately upon loading. In contrast, asynchronous installation utilizes an initial spacing smaller than the chain length, with the chain arranged in a loop to prevent entanglement. The chain remains slack until the dragging process increases the anchor spacing to match the chain length. As shown in Figure 6b, the chain is modeled using cylindrical rigid-body elements designed to transmit only axial forces while maintaining constant distance between reference points.

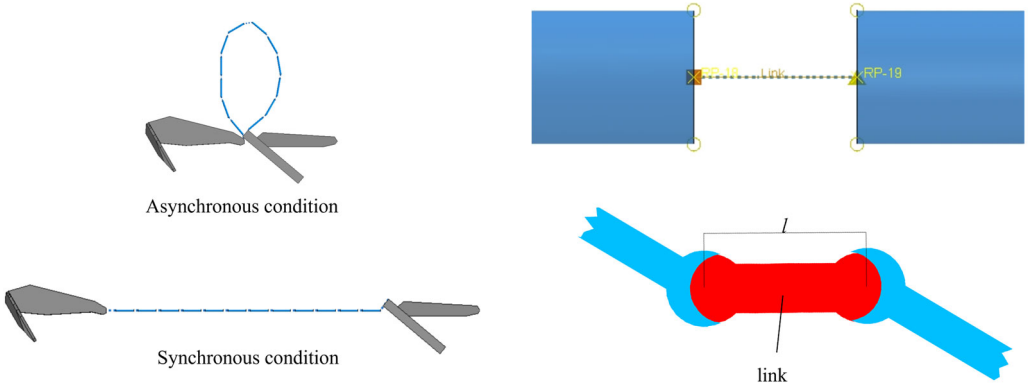


Figure 6. Linking chain configuration of GDAS: (**a**) linking chain layouts for synchronous and asynchronous installation methods and (**b**) mechanical property of the link connection.

2.5. Validation

To validate the hydro-mechanically coupled CEL method, two free-fall piezocone tests in soft clay from Reference [44] were simulated, accounting for large soil deformations and high strain rates. These 100 g centrifuge tests, conducted at the University of Western Australia, are ideal for validation due to their high-resolution pore-pressure measurements. The undrained shear strengths of the clay were s_u = 1.13z kPa and 1.17z kPa for samples 1 and 2, respectively. The model piezocone featured had a length of 120 mm, a 60° cone tip angle, a shaft diameter d of 10 mm and a total mass of 28.13 g. A pore-pressure transducer and a 1.3 mm-thick ring of polyethylene were located above the cone shoulder, as shown in Figure 7. A 30 mm water layer was maintained above the soil surface to ensure full saturation. The impact velocities were 4.7 m/s and 6.1 m/s for samples 1 and 2, respectively. A normalized numerical domain of 20 d × 20 d × 45 d was used to eliminate boundary effects, with calibrated VUMAT subroutine parameters detailed in Table 1.

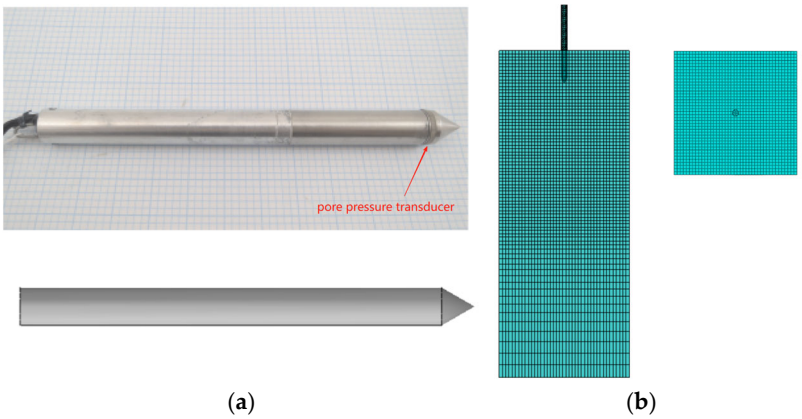


Figure 7. Free-fall piezocone test: (**a**) free-fall piezocone with pore-pressure transducer (after [44]) and numerical model; and (**b**) numerical domain for free-fall piezocone simulation.

Table 1. Parameters for VUMAT subroutine.

Parameters	Value
E	500 s_u
ν	0.49
k	1.5 kPa/m
K^{Perm}	1.0×10^{-5}
η^f	1.0×10^{-2}
φ^f	0.40
$\overline{K}^f$	2.2×10^9
S_t	2.0
ξ_{95}	50
μ_{10}	0.05
$\dot{\gamma}_{ref}$	0.1

Figure 8 compares the pore water pressure obtained from the numerical analyses with the measured results. The hydro-mechanically coupled CEL method effectively captures the general pore-pressure trends during high-velocity piezocone impact, including the excess pore-pressure overshoot observed at the end of penetration.

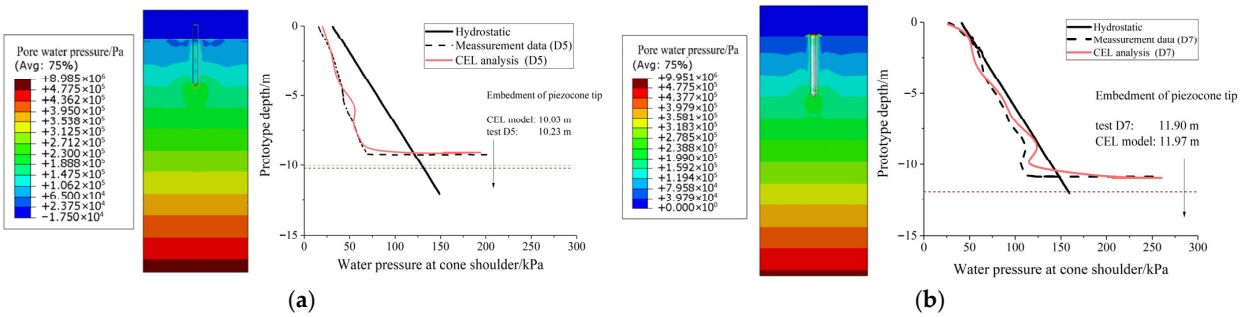


Figure 8. Comparison of pore water pressure between tests and numerical analyses: (**a**) sample 1, v_i = 4.7 m/s and (**b**) sample 2, v_i = 6.1 m/s.

To validate the GDAS installation model, numerical predictions were compared against 1 g laboratory results for the dual-anchor system from Reference [11]. Figure 9 illustrates the trajectories and tension results for the dual-anchor system in the soil with a shear-strength profile of s_u = 0.48 + 1.57z kPa. The length of linking cable between the two anchors was 5.4 L_f. With mean relative errors of 8.31% for trajectory and 4.14% for tension, the model accurately predicts the installation behavior of the dual-anchor system.

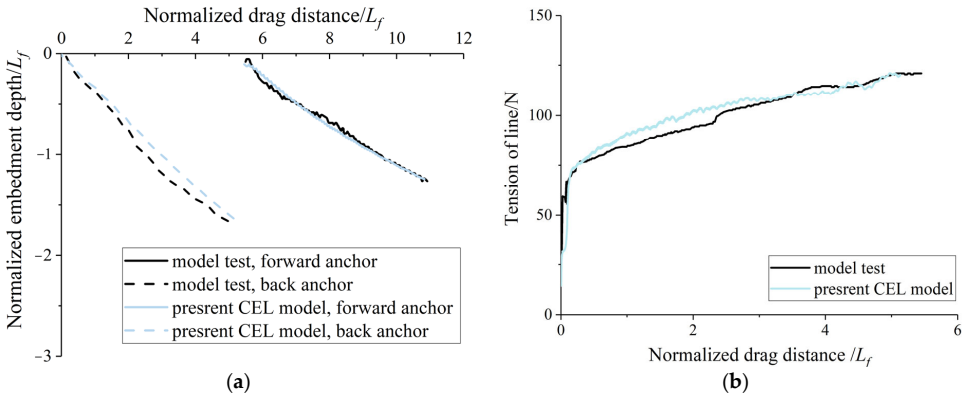


Figure 9. Comparison of results between 1 g test [11] and numerical analyses for group-drag-anchor installation: (**a**) trajectory of group-drag-anchor and (**b**) tension of line.

3. Analytical Cases

In this section, the analytical cases are designed to investigate the impact of asynchronous installation conditions on the embedment performance and dynamic response of the GDAS under cyclic loads, wave–current conditions and line-broken conditions.

3.1. Analytical Cases for Investigating the Influence of Asynchronous Installation Conditions

First, the effects of anchor spacing and soil-strength gradient on the GDAS's ultimate embedment were investigated. Table 2 outlines the analytical cases, which feature four normalized anchor spacings, such as 0 L_f, 2.5 L_f, 4 L_f and 5 L_f. With the GDAS's connecting-chain length set at 5 L_f, an anchor spacing of 5 L_f means the chain will be immediately taut once tension is applied to the padeye. This is defined as synchronous installation. An anchor spacing of 0 L_f represents fully asynchronous installation, where the connecting chain is initially slack. The 2.5 L_f and 4 L_f cases investigate the partially asynchronous effects, with 4 L_f specifically capturing nuances near the synchronous threshold. Additionally, three undrained shear-strength gradients of soil ranging from 0.5 kPa/m to 3.0 kPa/m are selected to cover the typical range encountered in offshore clay conditions [45].

Table 2. Analytical cases for investigating asynchronous installation effect.

Group Number	S_i/L_f	k (kPa/m)	Investigation Purpose
1	0, 2.5, 4.0, 5.0	0.5	Effect of asynchronous installation on the ultimate embedment depth of GDAS
2	0, 2.5, 4.0, 5.0	1.5, 3.0	Impact of soil-shear-strength gradient on the asynchronous installation effect

3.2. Analytical Cases for Investigating the Dynamic Response of GDAS

A critical consideration in storm loading analysis is the combined influence of two competing effects: the beneficial strain-rate effect, which temporarily enhances undrained shear strength, and the detrimental strength degradation induced by repeated cyclic loading. Building on the final positions from installation simulations, the GDAS's subsequent dynamic response is evaluated under three service scenarios. These scenarios include long-term cyclic mooring loads, combined wave–current loading, and sudden line failure. To simulate realistic in-service conditions several weeks post-installation, the clay is assumed to be fully reconsolidated, having recovered its virgin undrained shear-strength profile.

The designed cyclic loads are set by referencing the DNV standard [46]. According to the standard, the design line tension T_d can be expressed by two calculated line tension components,

$$T_d = T_{C\text{-}mean} \cdot \gamma_{mean} + T_{C\text{-}dyn} \cdot \gamma_{dyn} \quad (16)$$

where T_d is the design line tension; $T_{C\text{-}mean}$ denotes the characteristic mean line tension due to the pretension and the effect of mean environmental loads in the environment state; $T_{C\text{-}dyn}$ is the characteristic dynamic line tension equal to the increase in tension due to oscillatory low-frequency and wave-frequency effects; and γ_{mean} and γ_{dyn} are the respective partial safety factors. The values of these safety factors are determined by the consequence classes. Here, the class for the ultimate limit state representing the failure is unlikely to lead to unacceptable consequences, such as loss of life, and is selected for the subsequent analyses, i.e., γ_{mean} = 1.10 and γ_{dyn} = 1.50. The design line tension T_d is set as 14,500 kN, according to the project requirement of the offshore wind platforms in the south China sea area. Cyclic-loading frequencies of 0.05 Hz, 0.077 Hz and 0.15 Hz were selected to cover the typical range of peak wave periods observed in the region. Three dynamic tension amplitudes are investigated to represent a realistic spectrum of operational and extreme sea states. Additionally, the effect of asynchronous installation is examined under an extreme

storm scenario characterized by a cyclic tension amplitude four times the reference design value and a relatively high frequency of 0.5 Hz. Figure 10 illustrates the time histories of the cyclic tension applied at the mudline for all cases. The analytical cases are summarized in Table 3. The dynamic response of the GDAS is evaluated based on cumulative anchor displacement and pore water pressure characteristics after a 200 s loading period.

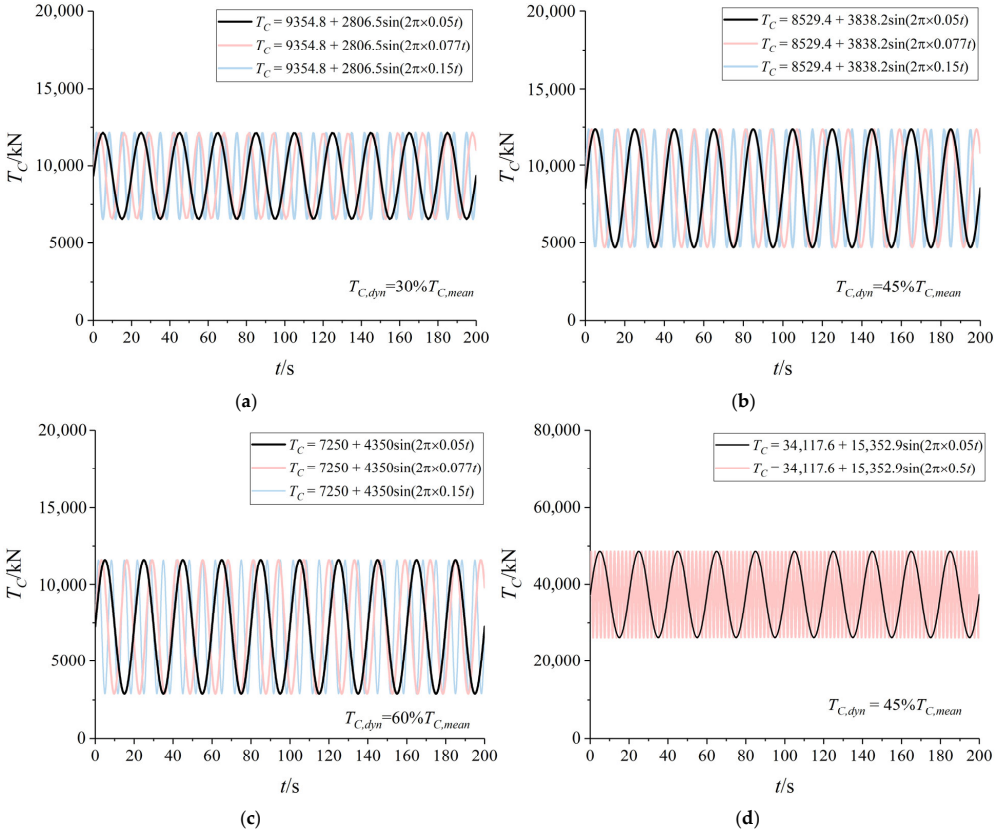


Figure 10. Time histories of mooring tension at mudline under regular cyclic loads: (**a**) $T_{C,mean}$ = 9354.8 kN, $T_{C,dyn}$ = 30%$T_{C,mean}$; (**b**) $T_{C,mean}$ = 8529.4 kN, $T_{C,dyn}$ = 45%$T_{C,mean}$; (**c**) $T_{C,mean}$ = 7250.0 kN, $T_{C,dyn}$ = 60%$T_{C,mean}$; and (**d**) $T_{C,mean}$ = 34,117.6 kN, $T_{C,dyn}$ = 45%$T_{C,mean}$.

Table 3. Analytical cases (regular cyclic loads).

Group	Installation Condition	k (kPa/m)	$T_{C,mean}$ (kN)	$T_{C,dyn}/T_{C,mean}$ %	Frequency (Hz)	Purpose	Number of Cases
1	synchronous; asynchronous	1.5; 3.0	9354.8, 8529.4, 7250.0	30; 45; 60	0.05; 0.077; 0.15	Effects of dynamic load proportion and frequency of cyclic loads	36
2	synchronous; asynchronous	1.5	34,117.6	45	0.05	Effect of asynchronous installation under extreme load	2
3	synchronous; asynchronous	1.5	34,117.6	45	0.5	Effect of asynchronous installation under extreme frequency (storm condition)	2

To evaluate the GDAS dynamic response under combined wave–current conditions, mooring-line tension histories from Reference [47] for a 5-MW offshore wind turbine were adopted, as shown in Figure 11. One of the load curves represents the tension under the wave-only condition. The other two load curves illustrate the tension variation under wave–current conditions with or without interaction. In their simulation, the wave–current interaction is achieved through a wave–current analytical model based on Airy's wave theory. The "wave–current with interaction" represents the condition that the current can alter the frequency and dispersion relationship of waves, leading to changes in wave height, wavelength, and

propagation speed, while the "wave–current without interaction" represents the wave load and current load calculated separately and then directly added together. Each 800 s time history was applied at the mudline to a GDAS installed either asynchronously (0 L_f) or synchronously (5 L_f). The detail analytical conditions are presented in Table 4.

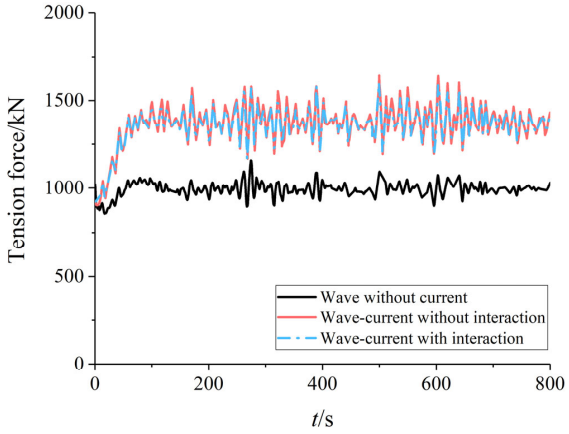


Figure 11. Time histories of mooring tension applied at mudline under wave–current loading conditions.

Table 4. Analytical cases (tension induced by wave–current loads).

Installation Conditions	*k* (kPa/m)	Load Conditions
synchronous; asynchronous	1.5	wave without current; wave–current without interaction; wave–current with interaction

Finally, the dynamic response of the GDAS was evaluated under damage-limit states representing mooring-line breakage. A series of tension time histories for a 5-MW floating offshore wind turbine subjected to various combinations of wave and wind directions that trigger line breakage were reported in Reference [48], as shown in Figure 12. Since the drag anchors cannot bear the tension in the opposite direction, only four cases (LC2, LC4, LC5, and LC10) without tension direction reversal are selected to investigate the response of the GDASs, as listed in Table 5. These cases also cover a representative range of post-failure tension characteristics, such as maintaining low level, moderate level, and high level and progressively increasing to moderate level. For each selected case, the tension time history, spanning 10 s before and 1000 s after the instant of line breakage, is applied at the mudline. This allows for a comprehensive assessment of both the transient impact and the long-term stability of the GDAS under realistic accidental loading.

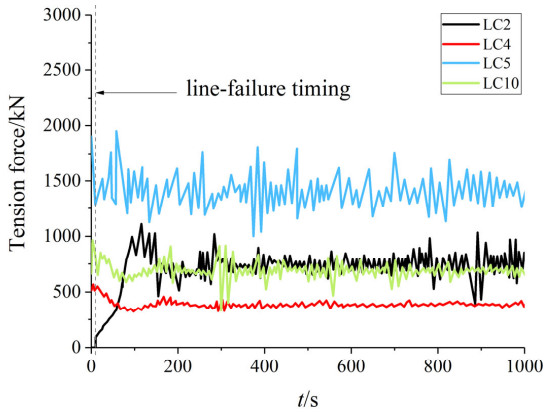


Figure 12. Time histories of mooring tension applied at mudline after adjacent line failure.

Table 5. Analytical cases (tension induced by line-failure conditions).

Installation Conditions	k (kPa/m)	Load Conditions
synchronous; asynchronous	1.5	LC2; LC4; LC5; LC10

4. Results and Discussion

4.1. Effect of Installation Anchor Spacing

Figure 13 shows the trajectory results of the GDAS under various asynchronous installation conditions. Asynchronous installation consistently yields greater embedment depths than the traditional synchronous method. However, in soft clay with a low undrained shear gradient (0.5 kPa/m), the performance gains across different degrees of asynchrony remain limited.

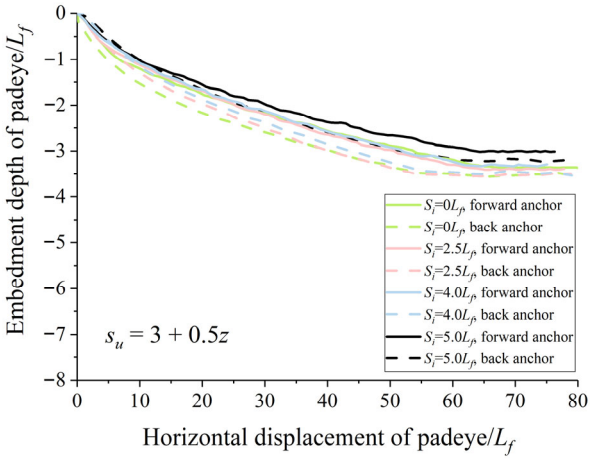


Figure 13. Trajectories of the GDAS under various asynchronous installation conditions.

Figure 14 compares the contours of equivalent plastic strain for the asynchronous (S_i = 0 L_f) and synchronous (S_i = 5 L_f) installation. The superior performance of the asynchronous approach can be attributed to three key mechanisms. First, it eliminates the interference from the back anchor during the initial penetration of the forward anchor, enabling smoother and deeper penetration of the forward anchor. Second, it reduces the effective resistance ahead of the trailing back anchor during penetration due to the preformed trench and disturbed soil zone created by the forward anchor. Third, once the chain tightens, the back anchor experiences a more favorable downward loading angle at its padeye, significantly enhancing its diving tendency and final depth.

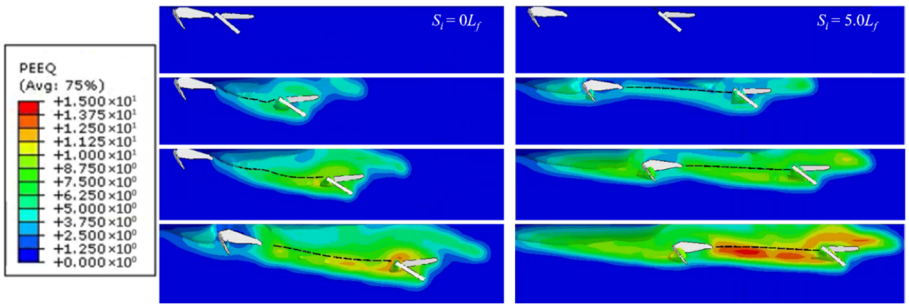


Figure 14. Soil-equivalent plastic strain under asynchronous and synchronous installation conditions.

4.2. Effect of Soil Property

In this section, the influence of soil-strength gradient on the effectiveness of asynchronous installation for the GDAS is analyzed in detail.

Figure 15a,b present the trajectory results of the GDAS under different asynchronous installation conditions in the seabed with an undrained shear-strength gradient of 1.5 kPa/m and 3.0 kPa/m, respectively. It can be observed that the beneficial effect of asynchronous installation becomes markedly more pronounced as the strength gradient increases. In the seabed with a shear-strength gradient of 1.5 kPa/m, asynchronous installation increases the final embedment depth of the forward anchor by 64.8 to 84.5% and the back anchor by 68.0 to 77.4%, relative to conventional synchronous installation, respectively. Furthermore, in the stiffer clay with 3 kPa/m, these improvements can be substantially greater, ranging from 105.9% to 233.8% for the forward anchor and from 91.2% to 182.4% for the back anchor.

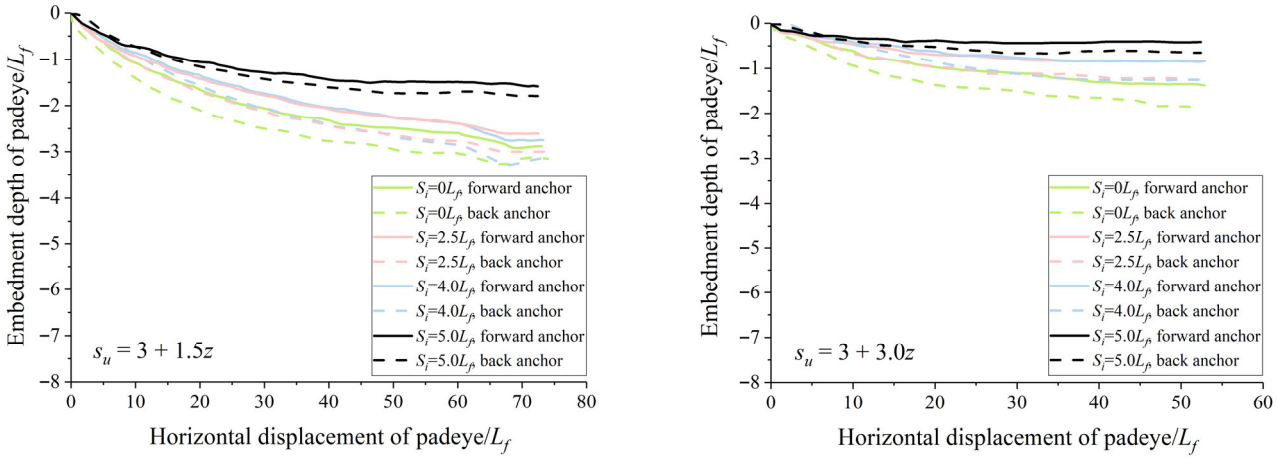


Figure 15. Effect of soil property on asynchronous installation impact: (**a**) s_u = 3 + 1.5z kPa and (**b**) s_u = 3 + 3.0z kPa.

These results demonstrate that the performance advantage of asynchronous installation is significantly amplified in seabeds with steeper undrained shear-strength gradients.

4.3. Installation Impacts on the Dynamic Response Characteristics of GDAS

4.3.1. Dynamic Response Characteristics of GDAS Under Cyclic Loads

Figure 16 shows the displacement evolution of the asynchronously installed GDAS under cyclic mooring loads across varying frequencies and dynamic tension proportions. Figure 16a,b present the horizontal and vertical displacements of the GDAS in the seabed with an undrained shear-strength gradient of 1.5 kPa/m, respectively. It can be observed that at low frequencies (0.05 Hz and 0.077 Hz), the horizontal displacement of the GDAS decreases noticeably as the dynamic tension proportion increases. This trend vanishes at the highest frequency (0.15 Hz). Conversely, vertical displacement remains largely insensitive to both frequency and dynamic proportion. Figure 16c,d present the corresponding results for a stiffer seabed with an undrained shear-strength gradient of 3.0 kPa/m. The forward anchor exhibited greater horizontal displacement than the back anchor. The forward anchor embedded deeper in seabed, while the back anchor experienced embedment loss. This differential behavior becomes significantly more pronounced as the dynamic tension proportion increases.

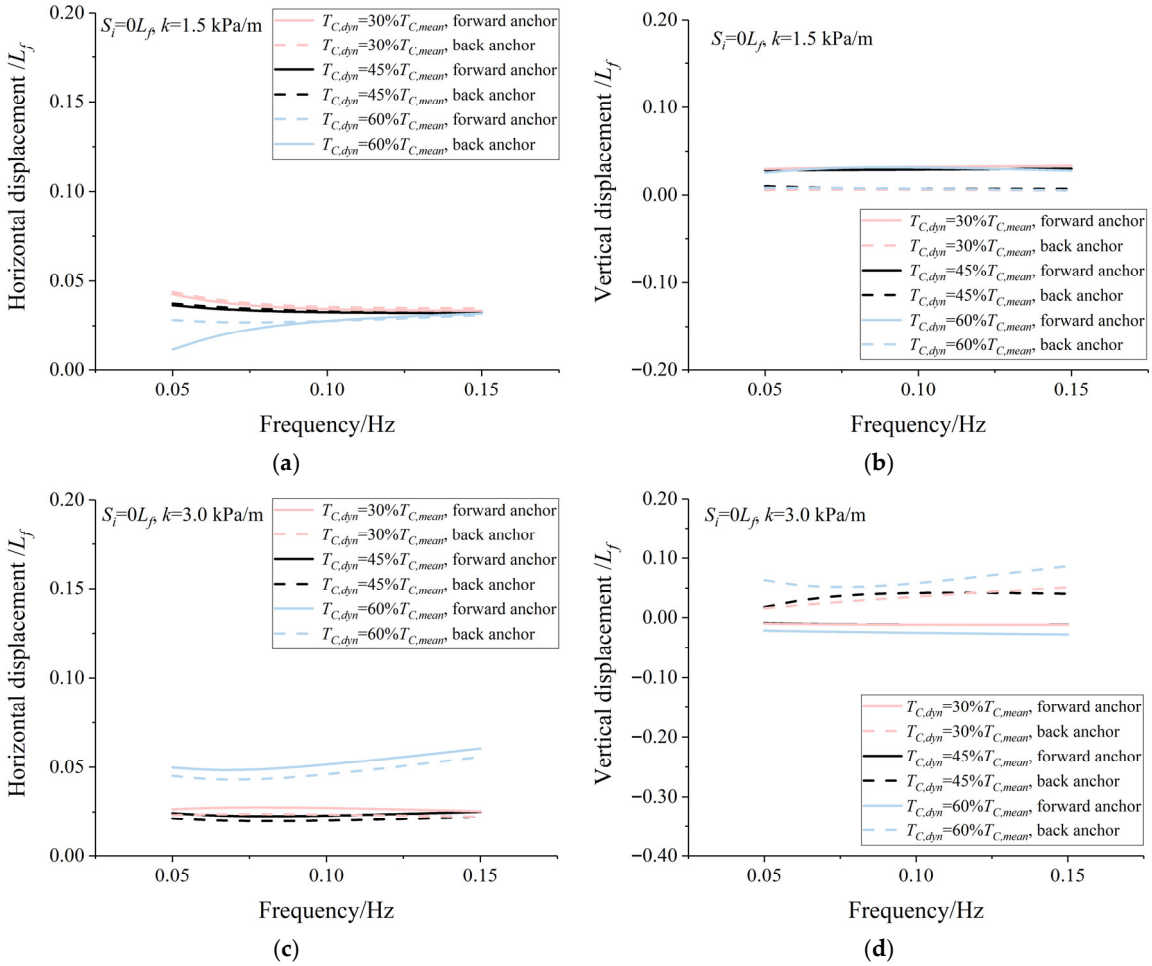


Figure 16. Displacement evolution of GDAS installed by asynchronous method under cyclic loads: (**a**) horizontal displacement, k = 1.5 kPa/m; (**b**) vertical displacement, k = 1.5 kPa/m; (**c**) horizontal displacement, k = 3.0 kPa/m; and (**d**) vertical displacement, k = 3.0 kPa/m.

Figure 17 shows the displacement evolution of synchronously installed GDASs under cyclic mooring loads across varying frequencies and dynamic tension proportions. Figure 17a,b present the horizontal and vertical displacements of GDASs in the seabed with an undrained shear-strength gradient of 1.5 kPa/m, respectively. Consistent with the behavior observed for asynchronously installed systems, horizontal displacement decreases with increasing dynamic tension proportion. Figure 17c,d present the response of a GDAS in a stiffer seabed with undrained shear-strength gradient of 3.0 kPa/m. The forward anchor embeds deeper in the seabed under the cyclic loads. The influence of loading frequency on overall displacement of the GDAS diminishes as the dynamic tension proportion increases. The results indicate that the shallower initial embedment from synchronous installation allows for greater mobilization under cyclic loads. The system's behavior reflects competition between strain-rate enhancement and strength degradation from cyclic loading. Lower dynamic load proportions allow frequency to dictate displacement, while higher proportions homogenize displacement by prioritizing amplitude-driven strain-rate strengthening. This coupling is more evident in stiffer soils (k = 3.0 kPa/m), where shallower initial embedment exacerbates mobilization.

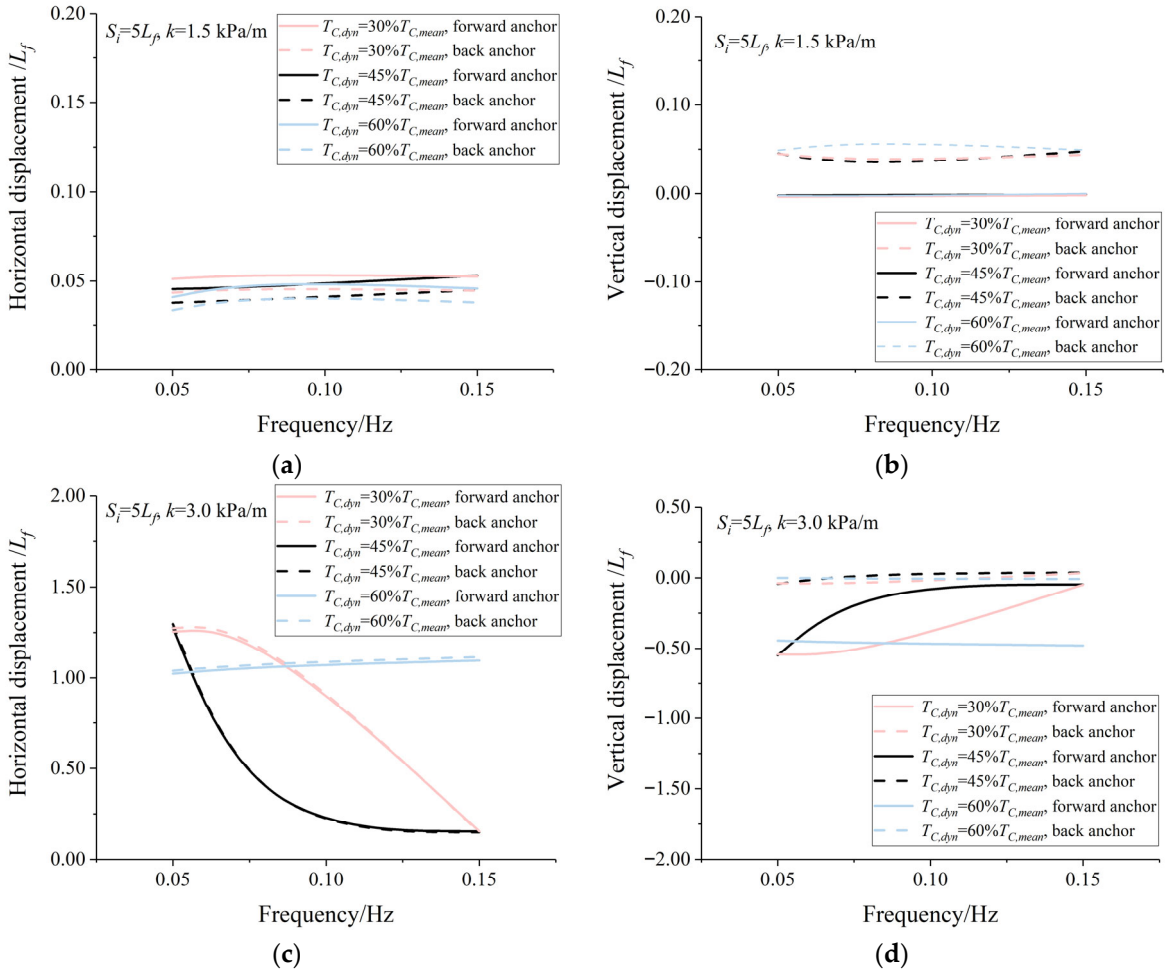


Figure 17. Displacement evolution of GDAS installed by synchronous method under cyclic loads: (**a**) horizontal displacement, k = 1.5 kPa/m; (**b**) vertical displacement, k = 1.5 kPa/m; (**c**) horizontal displacement, k = 3.0 kPa/m; and (**d**) vertical displacement, k = 3.0 kPa/m.

Table 6 shows the displacement evolution and embedment loss percentages for asynchronous (S_i = 0 L_f) versus synchronous GDAS installation in a soft seabed (k = 1.5 kPa/m) across various cyclic-loading frequencies.

Table 6. Comparison of dynamic response between GDASs installed by synchronous and asynchronous methods (k = 1.5 kPa/m).

$T_{C,dyn}/T_{C,mean}$	Anchor Component	Frequency /Hz	Horizontal Displacement/L_f		Vertical Displacement/L_f		Embedment Loss/%	
			S_i = 0 L_f	S_i = 5 L_f	S_i = 0 L_f	S_i = 5 L_f	S_i = 0 L_f	S_i = 5 L_f
30%	Forward anchor	0.05	0.042	0.051	0.029	−0.004	1.00	−0.26
		0.1	0.034	0.053	0.032	−0.003	1.10	−0.19
		0.15	0.032	0.052	0.032	−0.002	1.10	−0.13
	Back anchor	0.05	0.043	0.043	0.005	0.044	0.16	2.46
		0.1	0.035	0.045	0.006	0.039	0.19	2.18
		0.15	0.035	0.045	0.006	0.045	0.19	2.52
60%	Forward anchor	0.05	0.027	0.041	0.025	−0.003	0.86	−0.19
		0.1	0.027	0.048	0.031	−0.002	1.07	−0.13
		0.15	0.031	0.046	0.026	0.001	0.90	0.06
	Back anchor	0.05	0.011	0.033	0.007	0.048	0.22	2.68
		0.1	0.027	0.040	0.007	0.055	0.22	3.08
		0.15	0.032	0.038	0.005	0.050	0.16	2.80

Under a cyclic load with a 30% dynamic tension proportion, the GDAS response varies significantly by installation method. It can be observed that for the GDAS installed by the asynchronous installation method, the horizontal displacements for both anchors decrease as the loading frequency increases, eventually stabilizing. Embedment depth

exhibits minimal reduction, largely independent of frequency, with the forward anchor showing slightly more reduction than the back anchor. However, for the GDAS installed in synchronous conditions, horizontal displacement is higher than in asynchronous cases and remains largely insensitive to frequency variations. While the forward anchor achieves slightly deeper embedment under these loads, the back anchor suffers a much more significant embedment loss compared to the asynchronous condition.

Under cyclic loading with a 60% dynamic tension proportion, for the asynchronous installation condition, the loading frequency has a negligible effect on the displacement of the forward anchor, while the lower loading frequency can noticeably reduce the horizontal displacement for the back anchor. For the synchronous installation, the lower loading frequency decreases the displacements for both the forward and back anchors.

Comparative analysis of embedment loss percentages confirms that asynchronously installed GDASs provide superior long-term stability. In relatively soft clay, this method yields a significantly lower maximum embedment loss percentage compared to traditional synchronous installation.

Table 7 shows the displacement response and the embedment loss percentages of the GDAS installed in a stiffer seabed with an undrained shear-strength gradient of 3.0 kPa/m under cyclic mooring loads at varying frequencies.

Table 7. Comparison of dynamic response between GDASs installed by synchronous and asynchronous methods (k = 3.0 kPa/m).

$T_{C,dyn}/T_{C,mean}$	Anchor Component	Frequency/Hz	Horizontal Displacement/L_f		Vertical Displacement/L_f		Embedment Loss/%	
			S_i = 0 L_f	S_i = 5 L_f	S_i = 0 L_f	S_i = 5 L_f	S_i = 0 L_f	S_i = 5 L_f
30%	Forward anchor	0.05	0.028	1.249	−0.012	−0.541	−0.89	−127.74
		0.1	0.028	0.887	−0.012	−0.374	−0.89	−88.31
		0.15	0.028	0.147	−0.010	−0.047	−0.74	−11.10
	Back anchor	0.05	0.021	1.272	0.016	−0.039	0.86	−6.04
		0.1	0.021	0.894	0.036	−0.017	1.94	−2.63
		0.15	0.021	0.157	0.053	0.036	2.86	5.58
60%	Forward anchor	0.05	0.048	1.019	−0.021	−0.444	−1.56	−104.84
		0.1	0.051	1.073	−0.027	−0.468	−2.00	−110.51
		0.15	0.061	1.095	−0.027	−0.476	−2.00	−112.40
	Back anchor	0.05	0.045	1.041	0.063	0.003	3.40	0.46
		0.1	0.045	1.090	0.059	−0.007	3.18	−1.08
		0.15	0.055	1.118	0.087	−0.007	4.70	−1.08

Under a 30% dynamic tension proportion, a GDAS's response in stiff soil (k = 3.0 kPa/m) varies by installation method. For the asynchronously installed GDAS, horizontal displacement is largely insensitive to frequency. As frequency increases, the back anchor suffers greater embedment loss. However, the synchronously installed GDAS is highly sensitive to frequency, exhibiting significantly larger horizontal displacements at low frequencies (e.g., 0.05 Hz). Under these conditions, the forward anchor dives to much greater depths. As frequency increases, the additional embedment depth for the forward anchor progressively diminishes, while the back anchor experiences embedment loss under high frequency conditions.

At a 60% dynamic tension proportion, the GDAS's response in stiff soil reveals a clear performance gap based on the installation method. The asynchronously installed GDAS exhibits excellent stability, characterized by small displacements and is largely insensitive to changes in loading frequency. However, GDASs installed via the synchronous method exhibit markedly greater sensitivity to cyclic loading, resulting in significantly larger displacements. The variation in loading frequency has a minimal influence on the GDAS's displacement for both synchronous and asynchronous installation methods. These results clearly demonstrate that asynchronously installed GDASs obtain a substantially more stable operational state under intense cyclic mooring loads, with the advantage being particularly evident in high-amplitude, storm-like conditions.

Table 7 indicates that synchronously installed GDASs allow the forward anchor to undergo significant additional embedment, partially compensating for its shallow initial depth. However, the back anchor experiences substantially less additional embedment than the forward anchor. In contrast, the asynchronously installed GDAS demonstrates superior stability, with a notably smaller difference in embedment depths between the forward and back anchors.

GDASs installed via the synchronous method are more easily mobilized by low-frequency cyclic loading in seabeds with steep strength gradients. This is primarily attributed to their shallower initial embedment. Low-frequency loads effectively trigger the system's latent capacity for further embedment. The partially installed GDAS, due to its synchronous installation, also demonstrates the hypothesis proposed in Reference [34], which states that partially installed drag anchors tend to embed deeper and develop enhanced holding capacity when subjected to extreme loads. Conversely, the asynchronously installed GDAS attains considerably greater initial embedment depths, placing both anchors in stronger soil. Consequently, it exhibits substantially greater resistance to cyclic mobilization and maintains a markedly more stable operational state throughout its service life.

Figure 18 illustrates the evolution of excess pore water pressure around the GDASs installed via asynchronous and synchronous methods. The markedly different initial embedment depths of the two methods strongly dictate the subsequent pore-pressure response. As embedment depth increases, both the amplitude and rate of excess pore-pressure accumulation decrease, while dissipation time increases, resulting in a progressively more uniform spatial distribution. Notably, the synchronously installed GDAS shows significant positive and negative excess pore pressures on opposite sides of the anchor plate, indicating a clear bipolar distribution. This asymmetric distribution reflects the intense localized soil flow and partial drainage around the shallower anchor during cyclic loading.

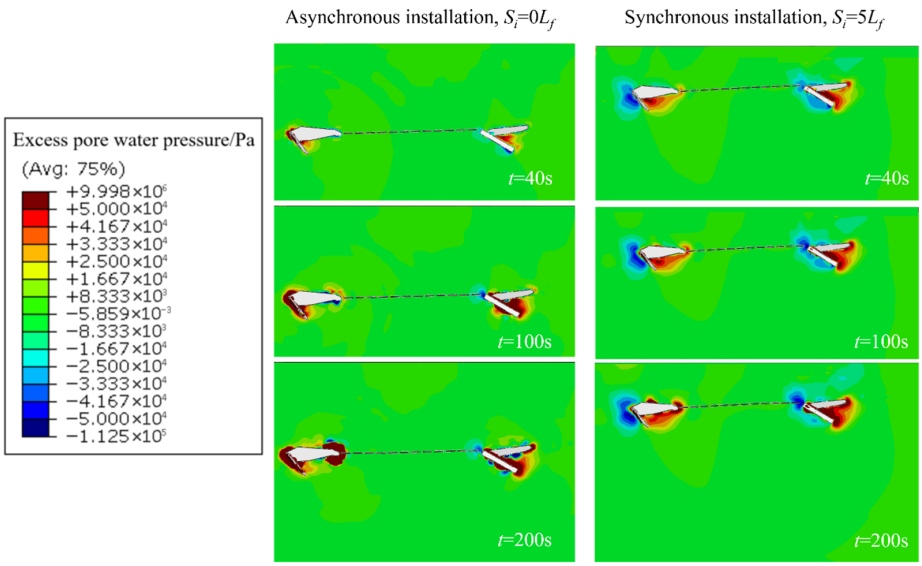


Figure 18. Evolution of excess pore water pressure around GDASs installed by asynchronous and synchronous methods ($T_{C,dyn}$ = 30%$T_{C,mean}$, f = 0.05 Hz).

Figure 19 compares the evolution of excess pore water pressure for asynchronously installed GDASs across various cyclic-loading frequencies. The results reveal only minor differences in excess pore-pressure response around the GDAS within this typical frequency range. By combining the results in Figure 16, these findings indicate that the asynchronous GDAS maintains a more stable service state. It effectively mitigates excess-pore-water-driven degradation through rate-enhanced soil resistance under high-frequency loads.

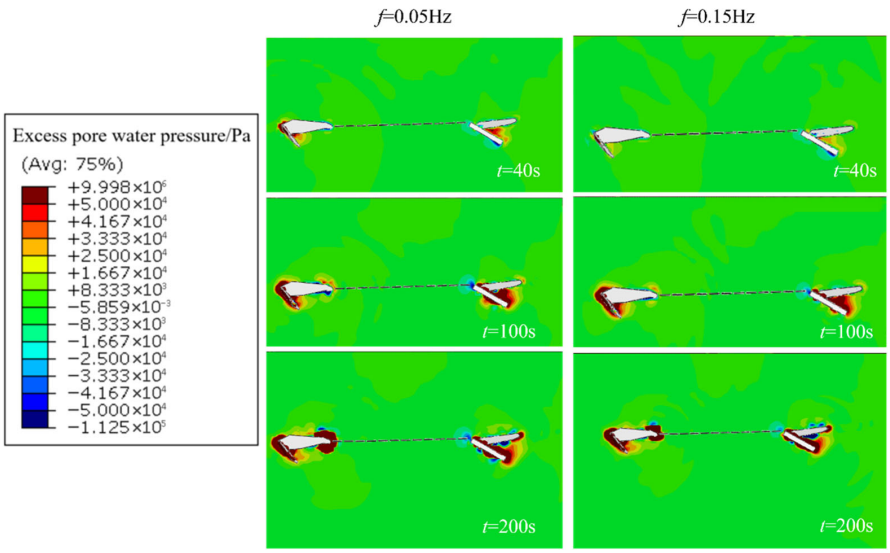
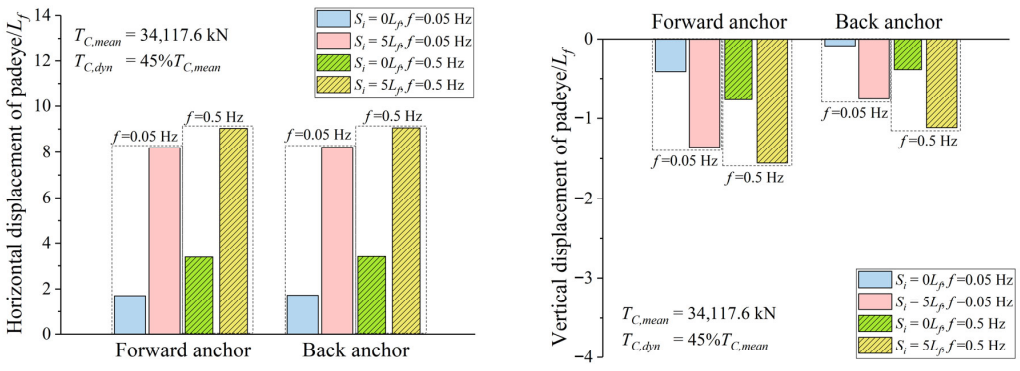


Figure 19. Evolution of excess pore water pressure around GDASs installed by asynchronous method under various cyclic-loading frequencies.

Figure 20 presents the displacement response of the GDAS under extreme storm loading, which combines very large tension amplitudes with high frequency. Both the asynchronously and synchronously installed systems exhibit progressive diving, resulting in a gradual increase in embedment depth throughout the storm event. Despite the higher loading frequency and correspondingly larger horizontal displacements, the vertical embedment continues to increase, confirming the inherent self-embedment capacity of GDASs when subjected to overloads. Moreover, the additional penetration is significantly more pronounced in the synchronously installed GDAS, which, due to its shallower initial embedment, achieves significantly greater additional embedment depth during the storm. These results demonstrate that the GDAS retains excellent holding capacity and can even enhance its long-term performance under extreme loads, providing a valuable safety margin. However, it should be noted that when the anchor deviates closer to the floating modules along the mooring projection direction, the maximum horizontal motion of the modules may gradually increase. When the anchor moves closer to the floating modules along the mooring projection direction, the connected line may gradually slacken, and the maximum mooring tension shifts to adjacent lines [49]. Therefore, the beneficial self-embedment capacity of the GDAS must be evaluated within the context of the entire mooring system to ensure global stability and avoid unintended consequences on platform responses.



(**a**) (**b**)

Figure 20. Displacement of GDASs installed by synchronous and asynchronous methods under extreme load: (**a**) horizontal displacement of GDAS and (**b**) vertical displacement of GDAS.

4.3.2. Dynamic Response Characteristics of GDASs Under Wave–Current Conditions

Figure 21 compares the horizontal and vertical displacements of GDASs under wave-only, wave–current without interaction and wave–current with interaction conditions for both installation methods. The results show that wave–current variations have limited impact on overall GDAS displacement. The asynchronously installed GDAS experiences more embedment loss, especially for the forward anchor. This is primarily attributed to the initial deeper embedment depth during the initial diving process due to sufficient mobilization of the GDAS's embedment potential. The deeper and harder soil around the GDAS makes the embedment creep more prominent under the influence of environmental loads. It provides immense resistance and prevents the forward anchor from dragging horizontally, instead causing it to rotate around a point. Even if the peak tension never exceeds the GDAS's ultimate capacity, the repeated loading induced by environmental loads triggers the embedment loss of the GDAS.

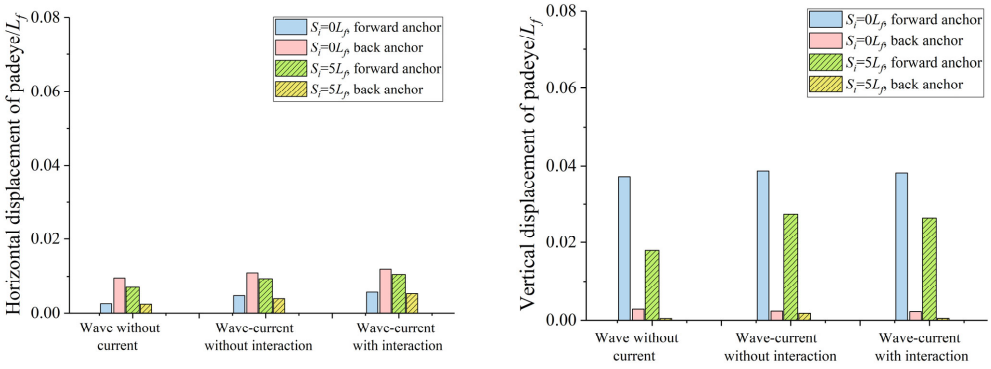


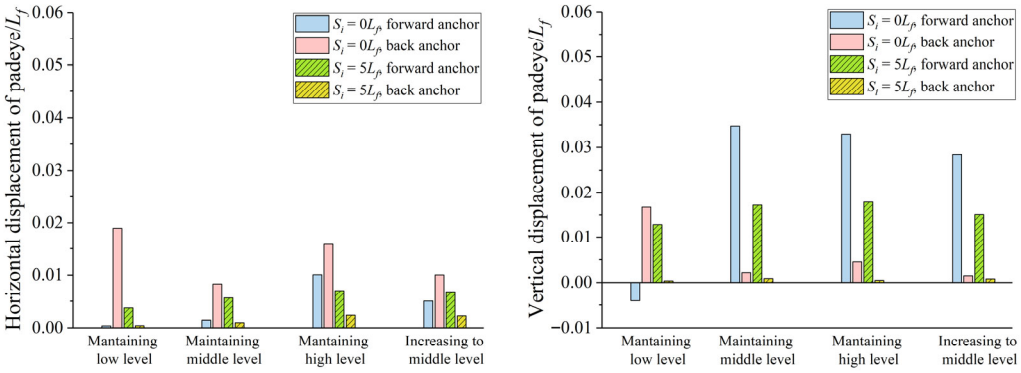
Figure 21. Displacement of GDASs under various wave–current load conditions: (**a**) horizontal displacement of GDAS and (**b**) vertical displacement of GDAS.

The results reveal that the wave–current loading case without hydrodynamic interaction represents the most dangerous condition for the GDAS, although the resulting anchor displacements are only marginally larger than those under wave-only or fully interacted wave–current loading.

4.3.3. Dynamic Response Characteristics of GDASs Under Line-Broken Conditions

Figure 22 shows the displacement of GDASs under various line-break scenarios. It can be observed that under the middle and high loading levels, both asynchronously and synchronously installed systems exhibit significant embedment loss at the forward anchor, while the back anchor remains relatively stable. However, under low-level post-failure loading tensions, the asynchronously and synchronously installed GDASs exhibit distinctly different responses. For the synchronously installed GDASs, both the horizontal and vertical displacements are similar to those under the middle-level and high-level loading conditions, but with reduced magnitude. In contrast, the asynchronous installation promotes slight embedment gain for the forward anchor but causes embedment loss for the back anchor. This differential behavior ultimately degrades the overall bearing capacity of the GDAS, as the minor embedment increase in the forward anchor fails to offset the capacity reduction from the back anchor's embedment loss. The characteristic of the transient and long-term post-failure behavior can be clearly revealed by the comparison of LC2 and LC10 line-failure conditions, representing maintaining middle-level tension and increasing to middle-level tension, respectively. The initial line-failure stage for the LC2 (increasing to middle-level tension) reduces the embedment loss for both asynchronously

and synchronously installed GDASs. However, the higher peak tension in the LC2 time history produces a greater horizontal displacement for the GDAS. Thus, the displacement of GDASs is largely determined by the average and peak tension levels in the equilibrium state after cable breakage.



(**a**) (**b**)

Figure 22. Displacement of GDASs under tension load induced by various line-broken conditions: (**a**) horizontal displacement of GDAS and (**b**) vertical displacement of GDAS.

4.4. Limitations

Although the present results provide valuable insights into the effects of asynchronous installation on the GDAS's performance, the general applicability of the findings is limited by several key assumptions, including full reconsolidation prior to dynamic loading, isotropic initial stress conditions, constant permeability, idealized linear strength gradients, and neglect of anisotropy and full three-dimensional effects.

Current dynamic analyses assume full soil reconsolidation and strength recovery prior to loading. In practice, partial reconsolidation is more realistic, leaving the soil in a softer state with reduced undrained shear strength. Comparative results from soft versus hard clay seabeds suggest that, under partial reconsolidation, the asynchronously installed GDAS tends to exhibit larger horizontal displacements at relatively low dynamic tension proportions, but smaller displacements at high proportions. Meanwhile, embedment loss increases for the forward anchor while decreasing for the back anchor. These differential behaviors highlight the need to incorporate time-dependent reconsolidation effects in future modeling to better capture realistic long-term performance.

The assumptions of isotropic initial stress conditions and idealized linear strength gradients primarily influence the initial trajectory and ultimate embedment depth of the GDAS. While these simplifications may affect quantitative predictions, they are unlikely to fully negate the demonstrated advantages of asynchronous installation, such as superior embedment and operational stability. The constant permeability assumption has negligible impact on the installation phase (largely undrained), but it influences the dynamic response by controlling the accumulation and dissipation rates of excess pore water pressure. Nevertheless, the fundamental differences in pore-pressure characteristics between asynchronously and synchronously installed GDASs, such as amplitude, spatial distribution, and bipolar patterns, should remain qualitatively consistent.

Finally, the present modeling framework does not account for seabed anisotropy and full three-dimensional effects, including non-coplanar mooring forces and anchor rollover. These factors can significantly affect installation stability, trajectory, ultimate embedment depth, and dynamic response. Systematic investigations incorporating anisotropic constitutive models, full three-dimensional large-deformation analyses and field/centrifuge

validation are recommended for future work to address these limitations and enhance confidence in GDAS design for real offshore conditions.

4.5. Discussion

This study represents an advancement in offshore geotechnical engineering, particularly for mooring systems supporting floating offshore wind turbines (FOWTs) in challenging soft clay seabeds. The core contribution is the quantitative demonstration that asynchronous installation markedly outperforms synchronous installation. Asynchronous GDASs achieve deeper embedment, particularly in seabeds with steep strength gradients, positioning both anchors in stronger soil layers. This results in lower excess pore-pressure amplitudes, more uniform spatial distribution, and enhanced long-term operational stability. These findings offer direct engineering guidance for optimizing GDAS design, component selection, connection methods, and installation sequencing, facilitating more reliable construction techniques that fully leverage the asynchronous effect.

5. Conclusions

This study investigates the asynchronous installation effect on the embedment performance and dynamic response of a developed group-drag-anchor system (GDAS), comprising a Delta anchor (forward anchor) and a four-tooth anchor (back anchor), in a soft clay seabed. A large-deformation finite element model based on the coupled Eulerian–Lagrangian (CEL) technique was developed to predict the trajectories under various asynchronous installation conditions and undrained shear-strength gradients. Furthermore, a hydro-mechanically coupled CEL approach was employed to monitor pore-pressure evolution and analyze the mechanisms governing the system's response to environmental loads. Some remarks are summarized as follows:

When the initial anchor spacing is 0 L_f, with the back anchor's padeye adjacent to the forward anchor's tail, the GDAS maximizes its ultimate embedment depth by fully leveraging the asynchronous effect. This enhanced performance is due to the asynchronous process, which eliminates interference from the back anchor during the forward anchor's initial penetration and reduces effective resistance for the trailing back anchor.

For GDASs with insufficient initial embedment, cyclic loads, particularly at low frequency and small dynamic tension proportion, beneficially increase the forward anchor's depth. However, even with cyclic mobilization, synchronously installed GDASs remain shallower than those installed asynchronously.

Asynchronously installed GDASs demonstrate significantly greater operational stability than synchronous counterparts, particularly in seabeds with steep shear-strength gradients. Under extreme storm loads, the system exhibits robust self-embedment, providing a critical safety margin. For synchronously installed systems, this increase in embedment depth can exceed 1.0 L_f. In contrast, the asynchronously installed GDAS experiences less additional displacement, contributing to its superior stability. However, this beneficial diving behavior must be assessed within the full mooring system, as excessive anchor displacement can increase platform excursions and redistribute loads to adjacent lines, potentially compromising global system integrity.

Several key assumptions in the developed model can constrain the generalizability of the findings. These include full soil reconsolidation prior to dynamic loading, isotropic initial stress conditions, constant permeability, idealized linear strength gradients, and the neglect of soil anisotropy and full three-dimensional effects. While the asynchronous installation effect in sand is expected to resemble that in hard clay, dynamic responses may differ. To address these limitations and strengthen confidence in GDAS design for real

offshore scenarios, future work should incorporate anisotropic constitutive models, full three-dimensional large-deformation analyses, and field or centrifuge validation.

Author Contributions: Conceptualization, Y.Y. and Y.L.; methodology, Y.Y.; software, D.N.; validation, Y.Y.; formal analysis, Y.Y.; investigation, Y.Y. and Y.L.; resources, Y.Y.; data curation, Y.Y.; writing—original draft preparation, Y.Y.; writing—review and editing, Y.L. and D.N.; visualization, Y.Y.; supervision, Y.L. and D.N.; project administration, Y.Y. and Y.L.; and funding acquisition, Y.Y. All authors have read and agreed to the published version of the manuscript.

Funding: This research was funded by the Postdoctoral Fund Project of Shanghai Investigation, Design & Research Institute Co., Ltd. (No. 2024QT(831)-002), the China Postdoctoral Science Foundation (No. 2025M773169) and the Shanghai Post-doctoral Excellence Program (No. 2024467).

Data Availability Statement: The data presented in this study are available on request from the corresponding author.

Conflicts of Interest: Authors Yancheng Yang and Yifeng Lin were employed by the company Shanghai Investigation, Design & Research Institute Co., Ltd. The remaining authors declare that the research was conducted in the absence of any commercial or financial relationships that could be construed as a potential conflict of interest.

Nomenclature

a	size of minimum mesh
b	effective width of chain or cable
c	specific heat
c_d	dilatational wave speed of the material
d	cone diameter
d_l	diameter of anchor cable or chain
E	Young's modulus
E_n	multiplier depending on the anchor line property, E_n = 2.5 and E_n = 1.0 for chain and cable, respectively
f	frequency of cyclic load
g	gravity
k	gradient of soil shear strength
K_0	coefficient of earth pressure
$\overline{K}^f$	bulk modulus of the fluid
K^{Perm}	permeability of solid
L_e	characteristic element dimension
L_s	length of the finite element model domain
L_f	length of back anchor fluke
$\dot{m}_T$	heat production
N_{cl}	bearing capacity factor of the cable or chain
p^f	pore fluid pressure
$\dot{p}^f$	increasing rate of pore fluid pressure
Δp^f	variation in pore fluid pressure
S_i	anchor spacing at initial installation
S_t	soil sensitivity
s_u	undrained shear strength of soil
s_{u0}	undrained shear strength of at mudline
s_{ui}	initial undrained shear strength of soil
T_a	drag force applied at the padeye
T_C	line tension applied at mudline
$T_{C\text{-}mean}$	characteristic mean line tension
$T_{C\text{-}dyn}$	characteristic dynamic line tension
T_d	design line tension

t	time
t_c	time interval for tension updating
Δt_c	critical time step increment
$\dot{u}^f$	pore fluid velocity
$\dot{u}^s$	solid velocity
$\ddot{u}^s$	acceleration of solid
$\overline{v}$	mean horizontal velocity
v_c	control velocity
W_s	width of the finite element model domain
w	submerged line weight per unit length
w^f	Darcy velocity of the pore fluid
z	soil depth
z_a	depth of the anchor padeye
z_e	initial embedment depth of the anchor line due to the self-weight of the line
β_s	coefficient of soil softening
β_r	coefficient of soil strain rate
δ_{rem}	inverse of the soil sensitivity
ξ	current cumulative plastic strain of soil
ξ_{95}	cumulative plastic strain when the soil strength has decreased by 95%
φ^f	volume fraction of pore fluid
μ	Poisson's ratio
μ_0	friction coefficient at the anchor–clay interface
μ_{10}	coefficient of soil-strength growth rate every 10 years
μ_l	frictional coefficient between the soil and anchor cable
η^f	dynamic viscosity of the fluid
ρ	soil total density
$\overline{\rho}^f$	intrinsic density of the fluid
λ	thermal conductivity
θ	angle formed by the cable to the horizontal plane
θ_{ah}	angle of drag force at the padeye to the horizontal
θ_e	loading angle of chain at the mudline to horizontal
θ_T	temperature
$\dot{\theta}_T$	increasing rate of temperature
γ_{mean}	safety factor for characteristic mean line tension
γ_{dyn}	safety factor for characteristic dynamic line tension
$\dot{\gamma}_{max}$	maximum shear strain rate
$\dot{\gamma}_{ref}$	reference shear strain rate

References

1. Cerfontaine, B.; White, D.; Kwa, K.; Gourvenec, S.; Knappett, J.; Brown, M. Anchor geotechnics for floating offshore wind: Current technologies and future innovations. *Ocean Eng.* **2023**, *279*, 114327. [CrossRef]
2. Lai, Y.; Xiong, S.; Tao, P.; Huang, C.; Zhu, Q.; Shu, S.; Chen, H. Experimental investigation and optimization of piggy-backed anchors in clay. *Ocean Eng.* **2025**, *333*, 121513. [CrossRef]
3. Cerek, K.; Hadjiloo, E.; Grabe, J.; Dao, D.A. Optimization of drag embedment anchors applying multi-objective evolutionary algorithm NSGA-II. *J. Ocean Eng. Sci.* **2025**, *10*, 1019–1030. [CrossRef]
4. Miedema, S.; Lagers, G.; Kerkvliet, J. An overview of drag embedded anchor holding capacity for dredging and offshore applications. In Proceedings of the WODCON, Orlando, FL, USA, 27 May–1 June 2007.
5. Aubeny, C.P.; Chi, C.M. Mechanics of drag embedment anchors in a soft seabed. *J. Geotech. Geoenviron. Eng.* **2010**, *136*, 57–68. [CrossRef]
6. Lai, Y.; Chen, C.; Pan, A.; Zhu, B. Centrifuge modelling and the modified limit equilibrium prediction for drag embedment anchor installation in sand. *Appl. Ocean Res.* **2025**, *154*, 104390. [CrossRef]
7. Lai, Y.; Yang, M.; Chen, C.; Zhu, B.; Chen, Y. Experimental behavior of piggy-backed anchors in cohesionless soils. In Proceedings of the IOP Conference Series: Earth and Environmental Science, Shanghai, China, 26–29 May 2024; Volume 1337, p. 012048.

8. Lai, Y.; Chen, C.; Yan, Z.Z.; Zhu, B. The installation behavior and capacity of piggy-backed anchors for offshore wind turbine. *Sustain. Energy Technol. Assess.* **2024**, *70*, 103948. [CrossRef]
9. Walker, G.R.; Taylor, R.J. Model anchor tests in cohesionless soil. *J. Waterw. Port Coastal Ocean Eng.* **1984**, *110*, 463–471. [CrossRef]
10. Taylor, R.J.; True, D.; Arnold, F. Anchoring and mooring considerations for an OTEC pilot plant. In Proceedings of the OCEANS 2010 MTS/IEEE SEATTLE, Seattle, WA, USA, 20–23 September 2010; pp. 1–8.
11. Lai, Y.; Huang, Y.H.; Gilbert, R.B.; Aubeny, C.P. Behavior of piggy-backed drag embedment anchors in marine soils. *J. Geotech. Geoenviron. Eng.* **2022**, *148*, 04021167. [CrossRef]
12. Chen, H.R.; Gao, Y.F.; Shu, S. Kinematic behaviors of piggy-backed vertically loaded anchors in clay. *Acta Geotech.* **2024**, *20*, 1859–1876. [CrossRef]
13. Yang, Y.C.; Lin, Y.F.; Ning, D.Z. Numerical investigation on novel group-drag-anchor systems for soft clay seabed. *Results Eng.* **2025**, *27*, 106367. [CrossRef]
14. Dunnavant, T.W.; Kwan, C.T. Centrifuge modelling and parametric analyses of drag anchor behavior. In Proceedings of the Offshore Technology Conference, Houston, TX, USA, 3–5 May 1993.
15. O'Neill, M.; Randolph, M. Modelling drag anchors in a drum centrifuge. *Int. J. Phys. Model. Geo.* **2001**, *1*, 29–41. [CrossRef]
16. Liu, H.X.; Li, Y.; Yang, H.T.; Zhang, W.; Liu, C.L. Analytical study on the ultimate embedment depth of drag anchors. *Ocean Eng.* **2010**, *37*, 1292–1306. [CrossRef]
17. Harnois, V.; Parish, D.; Johanning, L. Physical measurement of a slow drag of a drag embedment anchor during sea trials. In Proceedings of the 4th International Conference on Ocean Energy, Dublin, Ireland, 17 October 2012.
18. O'Neill, M.P.; Bransby, M.F.; Randolph, M.F. Drag anchor fluke soil interaction in clays. *Can. Geotech. J.* **2003**, *40*, 78–94. [CrossRef]
19. Liu, H.X.; Zhao, Y.B. Numerical study of the penetration mechanism and kinematic behavior of drag anchors using a coupled Eulerian–Lagrangian approach. *Geotech. Eng.* **2014**, *45*, 29–39. [CrossRef]
20. Wu, X.N.; Chow, Y.K.; Leung, C.F. Prediction of drag anchor trajectory with both shallow and deep anchor behavior. In Proceedings of the Offshore Technology Conference Asia, Kuala Lumpur, Malaysia, 22–25 March 2016.
21. Zhao, Y.B.; Liu, H.X. Numerical implementation of the installation/mooring line and application to analyzing comprehensive anchor behaviors. *Appl. Ocean Res.* **2016**, *54*, 101–114. [CrossRef]
22. Qiao, D.S.; Bao, M.R.; Yan, J.; Zhou, D.C.; Li, Y.G. A method to predict embedded trajectory based on the finite element analyses of bearing capacity of drag anchor. In Proceedings of the International Conference on Offshore Mechanics and Arctic Engineering, Madrid, Spain, 17–22 June 2018; p. V009T010A005.
23. Bransby, M.F.; O'Neill, M.P. Drag anchor fluke-soil interaction in clays. In *Numerical Models in Geomechanics*; CRC Press: Boca Raton, FL, USA, 2020; pp. 489–494.
24. Qiao, D.S.; Guan, B.; Liang, H.Z.; Ning, D.Z.; Li, B.B.; Ou, J.P. An Improved method of predicting drag anchor trajectory based on the finite element analyses of holding capacity. *China Ocean Eng.* **2020**, *34*, 1–9. [CrossRef]
25. Shin, M.B.; Park, D.S.; Seo, Y.K. Effects of strain-softening and strain-rate dependence on the anchor dragging simulation of clay through large deformation finite element analysis. *J. Mar. Sci. Eng.* **2022**, *10*, 1734. [CrossRef]
26. Maitra, S.; Tian, Y.H.; Cassidy, M.J. Investigation of the installation process of drag-in plate anchors from LDFE modelling. *Géotechnique* **2024**, *74*, 1215–1227. [CrossRef]
27. Taylor, R.J.; Valent, P. *Design Guide for Drag Embedment Anchors*; Naval Civil Engineering Laboratory (USA): Port Hueneme, CA, USA, 1984.
28. Neubecker, S.R.; Randolph, M.F. The performance of drag anchor and chain systems in cohesive soil. *Mar. Georesour. Geotec.* **1996**, *14*, 77–96. [CrossRef]
29. Kim, B.M. Upper Bound Analysis for Drag Anchors in Soft Clay. Doctoral Dissertation, Texas A&M University, College Station, TX, USA, 2007.
30. Peng, J.S.; Liu, H.X. Analytical study on comprehensive behaviors of drag anchors in the seabed. *Appl. Ocean Res.* **2019**, *90*, 101855. [CrossRef]
31. O'Neill, M.P.; Grime, A.J.; Bransby, M.F.; Watson, P.G.; Whelan, J.R. A reliability-based assessment framework for drag anchors. *Can. Geotech. J.* **2024**, *61*, 2632–2652. [CrossRef]
32. Xu, M.T.; Zhou, W.J.; Zhang, S.H.; Guo, Z.; Rui, S.J. Integrated design model for dynamic uplift behavior of suction anchor. In Proceedings of the 5th International Symposium on Frontiers in Offshore Geotechnics, Nantes, France, 9–13 June 2025.
33. Takatani, T.; Maeno, Y.; Hiraishi, T.; Takayama, T. Dynamic Response of Seabed around Suction Anchor. *Proc. Civ. Eng. Ocean* **1994**, *10*, 207–212. [CrossRef]
34. Duong, M.T. An Investigation into the Performance of Anchors Under Dynamic Loading. Master's Thesis, The University of Western Australia, Perth, Australia, 2019.
35. Qiao, D.S.; Zhou, Y.C.; Xu, B.B.; Qin, J.M.; Tang, G.G.; Lu, L.; Ou, J.P. Dynamic response analysis of a fully coupled aerodynamic-hydrodynamic-mooring-anchor floating offshore wind turbine. *Ocean Eng.* **2024**, *312*, 119085. [CrossRef]

36. Xiao, Z.; Tian, Y.H.; Gourvenec, S. A practical method to evaluate failure envelopes of shallow foundations considering soil strain softening and rate effects. *Appl. Ocean Res.* **2016**, *59*, 395–407. [CrossRef]
37. Wang, D.; Hu, Y.X.; Randolph, M.F. Keying of rectangular plate anchors in normally consolidated clays. *J. Geotech. Geoenviron. Eng.* **2011**, *137*, 1244–1253. [CrossRef]
38. Neubecker, S.R.; Randolph, M.F. Performance of embedded anchor chains and consequences for anchor design. In Proceedings of the Offshore Technology Conference, Houston, TX, USA, 1–4 May 1995; pp. 191–200.
39. Zhao, Y.B.; Liu, H.X. An efficient approach to incorporate anchor line effects into the coupled Eulerian–Lagrangian analysis of comprehensive anchor behaviors. *Appl. Ocean Res.* **2016**, *59*, 201–215. [CrossRef]
40. Zhao, Y.B.; Liu, H.X. The drag effects on the penetration behavior of drag anchors during installation. *Ocean Eng.* **2015**, *109*, 169–180. [CrossRef]
41. Hamann, T.; Qiu, G.; Grabe, J. Application of a Coupled Eulerian–Lagrangian approach on pile installation problems under partially drained conditions. *Comput. Geotech.* **2015**, *63*, 279–290. [CrossRef]
42. Staubach, P.; Machaček, J.; Skowronek, J.; Wichtmann, T. Vibratory pile driving in water-saturated sand: Back-analysis of model tests using a hydro-mechanically coupled CEL method. *Soils Found.* **2021**, *61*, 144–159. [CrossRef]
43. Zienkiewicz, O.; Shiomi, T. Dynamic behaviour of saturated porous media; the generalized Biot formulation and its numerical solution. *IJNAM* **1984**, *8*, 71–96. [CrossRef]
44. Chow, S.H.; O'Loughlin, C.; Randolph, M. Soil strength estimation and pore pressure dissipation for free-fall piezocone in soft clay. *Géotechnique* **2014**, *64*, 817–827. [CrossRef]
45. Poulos, H.G. *Marine Geotechnics*; Routledge: London, UK, 1988.
46. DNV. *DNV-RP-E301*; Design and Installation of Fluke Anchors; Det Norske Veritas: Oslo, Norway, 2012.
47. Chen, L.; Basu, B. Wave-current interaction effects on structural responses of floating offshore wind turbines. *WiEn* **2019**, *22*, 327–339. [CrossRef]
48. Yang, R.Y.; Chuang, T.C.; Zhao, C.Y.; Johanning, L. Dynamic response of an offshore floating wind turbine at accidental limit states—Mooring failure event. *Appl. Sci.* **2022**, *12*, 1525. [CrossRef]
49. Du, J.F.; Zhang, D.Q.; Jin, T.; Zhu, F.S.; Yuan, Z.M.; Incecik, A. Dynamic response characteristics of floating offshore photovoltaic systems with anchor position deviations under extreme environmental conditions. *Phys. Fluids* **2025**, *37*, 027121. [CrossRef]

Disclaimer/Publisher's Note: The statements, opinions and data contained in all publications are solely those of the individual author(s) and contributor(s) and not of MDPI and/or the editor(s). MDPI and/or the editor(s) disclaim responsibility for any injury to people or property resulting from any ideas, methods, instructions or products referred to in the content.